Ultralow Surface Recombination Velocity in InP Nanowires Probed by Terahertz Spectroscopy

Hannah J. Joyce,*[†] Jennifer Wong-Leung,[‡] Chaw-Keong Yong,[†] Callum J. Docherty,[†] Suriati Paiman,[‡,§] Qiang Gao,[‡] H. Hoe Tan,[‡] Chennupati Jagadish,[‡] James Lloyd-Hughes,[†] Laura M. Herz,[†] and Michael B. Johnston*[†]

[†]Clarendon Laboratory, Department of Physics, University of Oxford, Oxford, OX1 3PU, United Kingdom
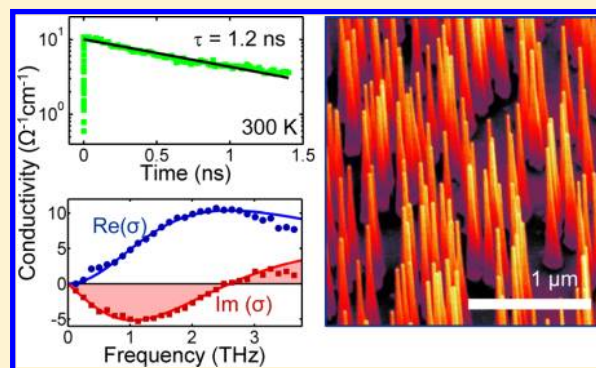
[‡]Department of Electronic Materials Engineering, Research School of Physics and Engineering, Australian National University, Canberra, ACT 0200, Australia

[§]Department of Physics, Faculty of Science, Universiti Putra Malaysia, 43400 Serdang, Selangor, Malaysia

S Supporting Information

ABSTRACT: Using transient terahertz photoconductivity measurements, we have made noncontact, room temperature measurements of the ultrafast charge carrier dynamics in InP nanowires. InP nanowires exhibited a very long photoconductivity lifetime of over 1 ns, and carrier lifetimes were remarkably insensitive to surface states despite the large nanowire surface area-to-volume ratio. An exceptionally low surface recombination velocity (170 cm/s) was recorded at room temperature. These results suggest that InP nanowires are prime candidates for optoelectronic devices, particularly photovoltaic devices, without the need for surface passivation. We found that the carrier mobility is not limited by nanowire diameter but is strongly limited by the presence of planar crystallographic defects such as stacking faults in these predominantly wurtzite nanowires. These findings show the great potential of very narrow InP nanowires for electronic devices but indicate that improvements in the crystallographic uniformity of InP nanowires will be critical for future nanowire device engineering.

KEYWORDS: InP, nanowire, terahertz, photoconductivity, surface recombination velocity, mobility

S emiconductor nanowires are predicted to drive new generations of compact, ultrafast, and high efficiency electronic and optoelectronic devices. Among nanowire materials, InP is especially promising due to its direct band gap and high electron mobility. A multitude of prototype InP nanowire devices have been demonstrated including photodetectors,[1] light-emitting diodes,[2] waveguides,[3] solar cells,[4,5] and field effect transistors.[2,6] Despite these early successes, there remain many fundamental unanswered questions concerning the dynamics of charge carriers in nanowires, and the effects of nanowire size, surfaces, and crystal structure on nanowire electronic properties. A greater understanding of these effects is essential for the future engineering of nanowire-based devices.

In this Letter, we examine the ultrafast carrier dynamics within InP nanowires and assess the effects of nanowire diameter, surfaces, and crystal structure. These investigations were performed using optical pump−terahertz probe (OPTP) spectroscopy, a technique which is ideally suited for nanowire studies because it is a noncontact ultrafast probe of room temperature photoconductivity with subpicosecond resolution.[7] The contact-free nature of this technique confers a significant advantage over conventional electrical transport measurements, which are subject to artifacts associated with electrical contacts and the models used to extract data.[8,9] A further advantage is that the OPTP measurements are performed at room temperature, so its measurements of carrier mobility and lifetime are directly relevant to future InP nanowire-based devices which will be operated at room temperature.

From OPTP measurements on InP nanowires of different diameters, we determine that surface recombination is negligible in InP nanowires. This result is despite the large surface area-to-volume ratio intrinsic to the nanowires and contrasts strongly with studies of GaAs nanowires for which surface recombination severely limits the carrier lifetime.[10] For InP nanowires we measured a long photoconductivity lifetime of over 1 ns. The long carrier lifetime at room temperature and insensitivity to surface states suggests that InP nanowires are excellent candidates for optoelectronic devices, especially for photovoltaic devices. Time-resolved PL spectroscopy was

performed in conjunction with OPTP measurements, and provided evidence that, after photoexcitation, electrons and holes are rapidly separated spatially into zinc-blende (ZB) and wurtzite (WZ) crystal sections, respectively, within the nanowires. This spatial separation of electrons and holes causes rapid PL quenching within 100 ps but allows a long carrier lifetime leading to long-lived photoconductivity. Additionally, we found that the carrier mobility does not show a simple systematic relationship with nanowire diameter. Instead, the carrier mobility is strongly influenced by the presence of planar crystallographic defects such as stacking faults, twins, and ZB–WZ polytypism in these predominantly WZ nanowires.

Nominally undoped InP nanowires were grown on InP (111)B substrates by metal–organic chemical vapor deposition (MOCVD) using Au nanoparticles to direct nanowire growth. Four samples were grown, each with Au nanoparticles of a particular nominal diameter (20, 30, 50, and 80 nm diameter). To eliminate the photoconductivity of the InP substrates, the nanowires were then transferred to z-cut quartz substrates by gently rubbing the two substrates together. Figure 1 illustrates scanning electron microscope (SEM) images of as-grown nanowires and nanowires on quartz. The nanowire diameters were measured from SEM images as described in the Supporting Information. The nanowire diameters depended on the diameter of the original Au nanoparticle plus a degree of tapering due to radial growth. Consequently each quartz
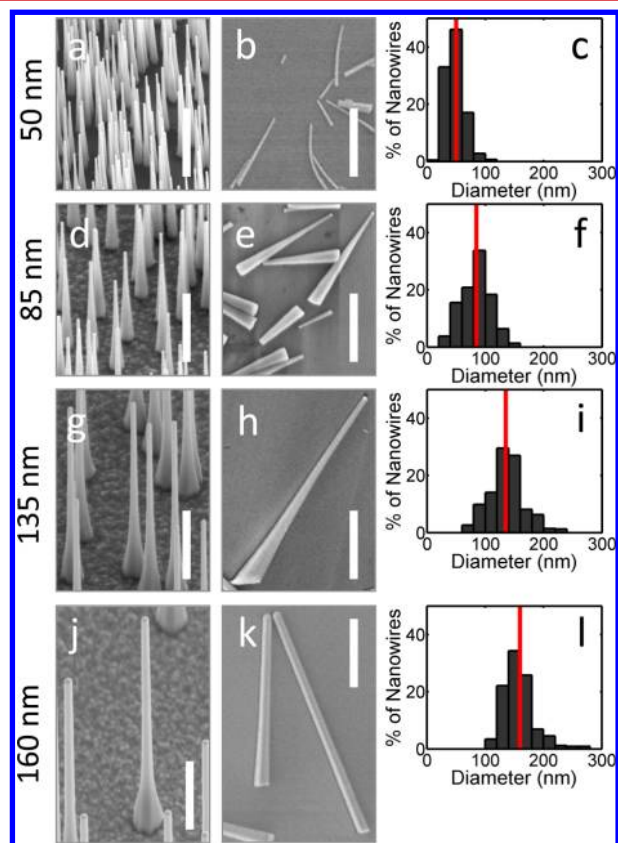
substrate hosted a distribution of nanowire diameters as summarized in the histograms of Figure 1. We hereafter refer to the samples by their average nanowire diameter after transferral to quartz substrates: 50, 85, 135, and 160 nm which respectively grew from the 20, 30, 50, and 80 nm diameter Au nanoparticles. A comparison of these four samples allowed the effects of nanowire diameter and surface-to-volume ratio to be examined.

The dynamics of photoexcited carriers were measured using the optical pump–terahertz probe spectroscopy setup described in the Supporting Information. The nanowires on quartz substrates were photoexcited using a pump pulse centered at a wavelength of 800 nm with a duration of 35 fs and fluence between 1 and 160 $\mu J/cm^2$. The photoexcitation induced a change ΔE in the transmission of a weak terahertz probe pulse E; this change in transmission is proportional to the photoinduced conductivity of the nanowires as discussed in the Supporting Information. Because the effective mass of holes in InP is significantly larger than that of electrons, we assume that the measured photoconductivity originated from photo-excited electrons only.

Nanowires have high surface area-to-volume ratios, and semiconductor surfaces tend to have high densities of dangling bonds which trap carriers and act as nonradiative recombination centers. Consequently, surface states are a major concern in nanowire engineering. Owing to the high aspect ratio of the nanowires, the sidefacets make the largest contribution to the surface area, whereas the top and bottom facets of the nanowires constitute only a minor portion of the nanowire surface (see Supporting Information). Nanowire diameter is the principal determinant of surface area-to-volume ratio. To assess the influence of surfaces on InP nanowires, we compare the photoconductivity lifetimes in each of the four samples of differing diameter, or equivalently, of differing surface-to-volume ratio. Figure 2a shows the decays of $\Delta E/E$ with time
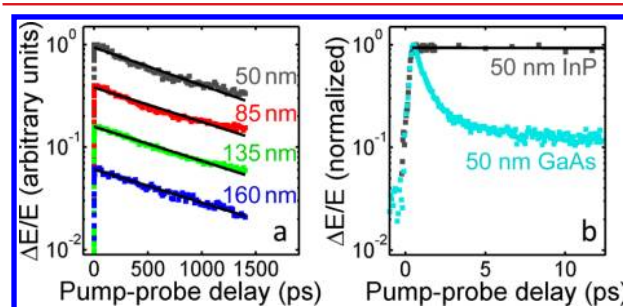

Figure 1. InP nanowires with average diameters of (a–c) 50 nm, (d–f) 85 nm, (g–i) 135 nm, and (j–l) 160 nm: a, d, g, and f are SEM images of InP nanowires as-grown on InP substrates at a tilt of 40°, b, e, h, and k are SEM images of InP nanowires transferred to quartz substrates, and c, f, i, and l are histograms of the diameters of nanowires on quartz. The average nanowire diameter for each sample is indicated in each histogram by the red line. SEM scale bars are 1 μm.

Figure 2. Pump-induced change in terahertz electric field ($\Delta E/E$) at different pump–probe delays. (a) $\Delta E/E$ decays for 50, 85, 135, and 160 nm diameter InP nanowires. These are scaled for clarity. (b) $\Delta E/E$ decays for 50 nm diameter InP nanowires and 50 nm diameter GaAs nanowires. The photoexcitation pump fluence was 8 $\mu J/cm^2$. Straight lines are monoexponential fits to the decays.

after photoexcitation for the four InP nanowire samples. The photoconductivity shows a rapid rise within 1 ps, followed by a slow decay. These data were fitted with an exponential function yielding time constants, τ, of 1.18 ns, 1.27 ns, 1.30 ns, and 1.34 ns, respectively, for the 50, 85, 135, and 160 nm diameter nanowires. Even the lowest diameter nanowires with the highest surface-to-volume ratio show a long photoconductivity lifetime. The weak dependence of photoconductivity lifetime on nanowire surface-to-volume ratio indicates that the carrier lifetime in InP nanowires is relatively insensitive to surface

states. This is consistent with the low surface recombination velocity of the InP material system.[11,12] As derived previously[13,14] and described in the Supporting Information, the effective recombination time is closely approximated by the function:

$$\frac{1}{\tau} = \frac{1}{\tau_{\text{volume}}} + \frac{4S}{d}$$

(1)

where d is the nanowire diameter, S is the surface recombination velocity, and τ_{volume} is the time constant for recombination at volume defects. By fitting eq 1 to the experimental τ values we extract a τ_{volume} of 1.4 ns and a surface recombination velocity of only 170 cm/s. This surface recombination velocity is consistent with results obtained for bulk n-InP.[11,15,16]

This result contrasts markedly with GaAs nanowires, as demonstrated in Figure 2b. The GaAs nanowires studied were of similar diameter to the 50 nm diameter InP nanowires, but the GaAs nanowires exhibit an extremely rapid initial decay in photoconductivity due to carrier trapping at surface states.[10] This is consistent with the high surface recombination velocity of GaAs.[12] Generally, surface passivation is essential to improve carrier lifetimes in GaAs nanowires.[17] InP nanowires, on the other hand, exhibit prolonged photoconductivity and a remarkably low electron trapping rate at surfaces, even without surface passivation. These findings are significant for many electronic applications which require long carrier lifetimes. In photovoltaic devices, for example, the long carrier lifetime and low surface recombination velocity would minimize recombination losses, to maximize the collected current and maximize energy conversion efficiency. We note that surface passivation of InP nanowires may yet be advantageous for light emission applications and photodiode devices, as demonstrated in previous studies.[5,18,19]

To further examine the carrier lifetimes, we performed room temperature time-resolved PL measurements using a PL up-conversion setup described in the Supporting Information. The sample was excited at 736 nm with pulses of 100 fs duration. Emitted PL was detected at the peak of the PL spectrum, at 870 nm (1.43 eV). This corresponds approximately to the band gap of WZ InP at room temperature as measured experimentally.[9,20,21] Figure 3a plots both the decay of $\Delta E/E$ and the decay of PL intensity for the same sample after photoexcitation with pulses of similar fluences. Interestingly, the PL decays rapidly with a decay time of only 30 ps, compared to the slow (>1 ns) decay time of $\Delta E/E$.

This apparent discrepancy relates to the fundamental differences between OPTP and PL measurements. OPTP spectroscopy measures the nanowire conductivity, whereas in PL spectroscopy, the PL intensity is proportional to the product of the electron and hole density distributions. The long OPTP lifetime suggests that photoexcited conduction electrons are present beyond 1 ns. The rapid quenching of PL within 100 ps suggests that the photoexcited electrons and holes contributing to conduction are spatially separated on this time scale and thereafter experience only a low radiative recombination rate. One explanation for this spatial separation is band bending at nanowire surfaces (see Supporting Information), but this effect is negligible in intrinsic and n-doped InP nanowires,[26] consistent with the very low surface recombination velocity we measure. Therefore the most likely root of spatial separation is the WZ–ZB polytypism present in the nanowire. The high resolution TEM images of Figure 3b
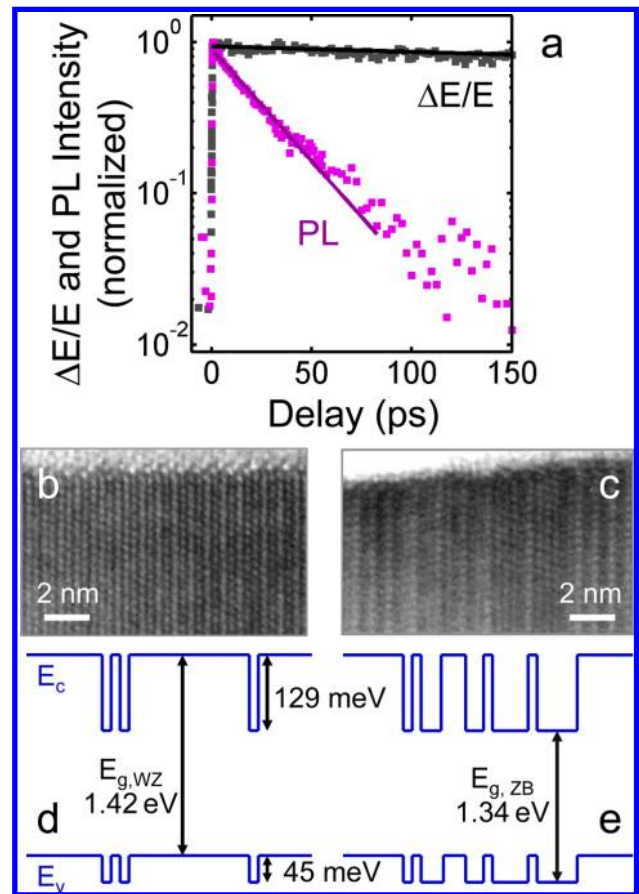

Figure 3. (a) Comparison of $\Delta E/E$ decay and time-resolved PL decay for 50 nm diameter InP nanowires. For all decays the photoexcitation pump fluence was approximately 8 μJ/cm². For PL measurements samples were photoexcited at 736 nm, and emitted PL was measured at 870 nm. For OPTP measurements samples were photoexcited at 800 nm. (b, c) HRTEM image of a typical InP nanowire (a) tip featuring predominantly WZ structure with stacking faults and (c) base with a higher density of stacking faults and thicker ZB segments. (d, e) Band diagrams at room temperature corresponding to nanowire (d) tip and (e) base. These band diagrams were constructed from published experimental and theoretical data for band gaps and band offsets.[9,20−25]

and c exemplify the crystal structure of these nanowires, which is predominantly WZ with thin ZB sections. These ZB sections vary in thickness between one bilayer (a single stacking fault) and up to eight bilayers. Nanowire tips exhibited lower densities of single stacking faults, whereas bases displayed a higher densities of stacking faults and thicker ZB sections. In WZ InP the conduction band is between 112 and 129 meV higher in energy, and the valence band is between 29 and 45 meV higher in energy than in ZB InP, as predicted theoretically[23−25] and observed experimentally.[22] This creates a type II junction between WZ and ZB sections of InP nanowires as illustrated in Figure 3d and e. After photo-excitation electrons and holes are rapidly separated into lower energy states in ZB and WZ sections, respectively. The spatial separation of electrons and holes causes a long carrier lifetime and low radiative recombination rate, consistent with our long OPTP lifetime and short PL lifetime. The short-lived PL we observe at 1.43 eV can be attributed to radiative recombination of electron−hole pairs residing in WZ sections of the nanowires, which is rapidly quenched due to localization of

electrons and holes into ZB and WZ sections, respectively. More long-lived red-shifted PL is expected from spatially separated electrons and holes, and this has been observed in low temperature PL measurements.[27,28]

Note that electrons and holes may still contribute to conduction despite their localization in ZB and WZ nanowire sections. In these predominantly WZ nanowires, the ZB segments are sufficiently thin, at less than 3 nm in thickness, that there is considerable leakage of the electron wave function into adjacent WZ segments.[25] The localization of electrons and holes could, however, result in increased scattering at boundaries between ZB and WZ segments and at stacking faults and consequently a reduced carrier mobility. To gain further insight into charge carrier scattering and mobility in these nanowires, we obtained photoconductivity spectra, as discussed in the following.

Figure 4 shows photoconductivity spectra collected for 50 nm InP nanowires. These were obtained at a delay of 20 ps after photoexcitation at various fluences. Spectra were also collected at various delays after photoexcitation, as presented in
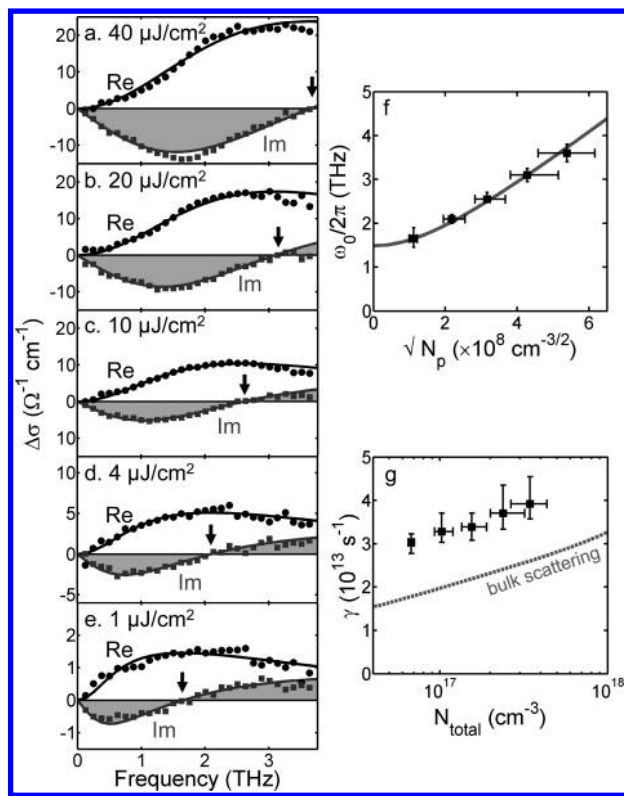

Figure 4. Fluence dependence of terahertz conductivity of 50 nm InP nanowires at 20 ps after photoexcitation. (a−e) Photoinduced conductivity of with pump fluences of (a) 40, (b) 20, (c) 10, (d) 4, and (e) 1 μJ/cm^2. The symbols are the measured data, and the lines are the fitted plasmon responses. The real (circles and lines) and imaginary (squares and lines) components of the conductivity are plotted. The arrow indicates the resonant surface plasmon frequency w_0. (f) Surface plasmon frequencies w_0 extracted from the fitted data (squares) and the fit (line) according to eq 3 with $f = 0.5$ and background electron concentration $N_d = 5.5 \times 10^{16}$ cm^{-3}. (g) Carrier scattering rates γ extracted from the fitted nanowire data (squares) and theoretically predicted for bulk InP (dotted line). The error bars indicate the uncertainty in N_p, N_{total}, w_0, and γ resulting from uncertainty in the measured fill fraction and in the parameters giving the optimum fits.

the Supporting Information. The conductivity spectra feature a pronounced Lorentzian response. The resonance shifts to higher frequencies with increasing photoexcitation fluence, as indicated by the arrows in Figure 4a−e. This fluence dependence is typical of localized surface plasmon modes, for which the resonant frequency depends on carrier density and, therefore, fluence.[29] Other processes may also give Lorentzian responses, for example, excitonic transitions and quantum confined states; however these would not show resonance shifts with fluence. We therefore attribute the response to a surface plasmon mode. This is consistent with previous work on GaAs nanowires, which also exhibit surface plasmon modes in the terahertz range.[10] The conductivity spectra were accordingly fitted with the function

$$\sigma = \frac{iN_p e^2 \omega}{m_e^*(\omega^2 - \omega_0^2 + i\omega\gamma)} \quad (2)$$

where N_p is the photoexcited carrier density, e is the electronic charge, m_e^* is the electron effective mass, ω_0 is the surface plasmon resonance, and γ is the momentum scattering rate. For m_e^* we use the value for bulk ZB InP of $0.08m_e$. This assumption is reasonable because temperature-dependent PL studies suggest the electron and hole effective masses are similar in both ZB and WZ InP,[21] and theoretical studies predict similar effective masses for ZB and WZ.[24,25,30] Fitting eq 2 to the conductivity spectra allowed parameters N_p, ω_0, and γ to be extracted.

The extracted surface plasmon frequency, ω_0, is plotted in Figure 4f, which clearly shows ω_0 shifts to higher frequencies with increasing carrier density. According to theory, the surface plasmon frequency is given by

$$\omega_0 = \sqrt{fN_{total}e^2/m_e^*\varepsilon_r\varepsilon_0} \quad (3)$$

where ε_r is the dielectric constant of the InP nanowires at terahertz frequencies, ε_0 is the permittivity of free space, and f is a constant dependent on the nanowire geometry and the surrounding dielectric medium.[31,32] We choose m_e^* and ε_r values for bulk ZB InP. Equation 3 closely fits the data using $f = 0.5$ and assuming the total carrier density N_{total} is the sum of two components, the photoexcited carrier density N_p and a constant background carrier density N_d due to doping. The fit shown in Figure 4f yields a moderate doping density of $N_d = 5.5 \times 10^{16}$ cm^{-3}. Although these nanowires are nominally undoped, this doping level is reasonable because the surface states are donors,[33] which will contribute to the electron density in the nanowires, and because these nanowires were grown at a low temperature at which donors such as phosphorus antisite defects are easily incorporated.[34]

Figure 4g plots the extracted scattering rates, γ, which vary between 3.0×10^{13} s^{-1} and 3.8×10^{13} s^{-1}, with a higher frequency of scattering events at higher carrier densities. From the scattering times the carrier mobilities can be calculated via

$$\mu = \frac{e}{m_e^*\gamma} \quad (4)$$

The extracted γ correspond to mobilities between 570 and 730 cm^2 V^{-1} s^{-1}. These values are significantly lower than typical electron mobilities of 6000 cm^2 V^{-1} s^{-1} in high quality InP epilayers.[35] Our data therefore suggest that additional carrier scattering processes dominate the transport of electrons in nanowires compared to bulk.

In bulk InP at room temperature, the dominant scattering processes are carrier–phonon, carrier–carrier, carrier–plasmon, and carrier–impurity scattering. These mechanisms result in theoretical scattering rates shown in Figure 4g, which were calculated using models outlined in previous publications[36,37] and as described in the Supporting Information. Both the experimental γ for nanowires and the theoretical γ for bulk InP show a similar dependence on carrier density, primarily due to increased carrier–carrier scattering at higher carrier densities. The experimental γ are, however, higher by approximately 1.3×10^{13} s^{-1}. This additional scattering component is constant, that is, not dependent on carrier density.

In nanowires, this additional scattering could arise from (i) roughness at nanowire surfaces and (ii) band offsets at planar crystallographic defects such as stacking faults, twins, and interfaces between ZB and WZ segments. To estimate the scattering contribution from (i), we refer to the model developed by Unuma et al. for quantum wells.[38] TEM images were analyzed from which we estimated the upper limit of the roughness height as 1 nm and estimated the lower limit of correlation length as 10 nm. This modeling revealed that surface roughness scattering is negligible for nanowire diameters larger than 20 nm, which is valid for all nanowire diameters studied here.

The modeling described above predicted that surface roughness scattering (i) has negligible influence on carrier mobility. This would imply that the nanowire surface area-to-volume ratio, and consequently diameter, should have a minimal effect on carrier mobility. To examine this prediction experimentally, we have measured photoconductivity spectra and extracted γ for the four samples of different diameters. The spectra are provided in the Supporting Information. For the 50, 85, 135, and 160 nm samples the scattering rates were approximately 3.3×10^{13} s^{-1}, 18×10^{13} s^{-1}, 10×10^{13} s^{-1}, and 4.5×10^{13} s^{-1}, respectively. These scattering rates correspond to mobilities of 660 cm^2 V^{-1} s^{-1}, 120 cm^2 V^{-1} s^{-1}, 220 cm^2 V^{-1} s^{-1}, and 480 cm^2 V^{-1} s^{-1}, respectively, for the 50, 85, 135, and 160 nm diameter samples. These mobilities show no systematic dependence on nanowire diameter: the 50 and 160 nm nanowires exhibit the highest mobilities, whereas the intermediate diameters exhibit the lowest mobilities. The nonsystematic variation in mobility suggests that other factors, for instance the density of stacking faults, plays a more dominant role in carrier dynamics than scattering at nanowire surfaces.

Assuming an electron thermal velocity of 4.1×10^7 cm/s, the measured scattering rates correspond to average scattering lengths, λ, between 2.3 and 12 nm (see Supporting Information). These lengths are considerably lower than the nanowire diameters studied here, supporting our observation that scattering at nanowire surfaces is not the major mechanism limiting carrier mobility. These scattering lengths are, however, comparable to the distances between planar crystallographic defects, as seen in the TEM images of Figure 3.

The most likely explanation for the low mobility in these nanowires is, therefore, the high density of stacking faults (ii). Recent publications on transport measurements of InP nanowire field effect transistors have alternately proposed that mobility is significantly degraded by stacking faults[8,39] or by surface scattering.[40] These studies, however, did not compare nanowires of different diameters. Our diameter-dependent measurements and theoretical calculations exclude the possibility of significant surface scattering, providing strong evidence that stacking faults limit nanowire conductivity.

The nonsystematic variation in mobility with nanowire diameter may be ascribed to differences in the density, distribution, and thickness of ZB segments from sample to sample. Such sample-to-sample variations in crystal structure are expected because the nanowire crystal structure is influenced by the nanowire diameter, and by a number of related parameters, such as nanowire growth rate and the density of Au nanoparticles on the substrate.[41,42] During nanowire growth these parameters act in conflicting ways to stabilize either ZB or WZ layers, so that the stacking fault density shows a complex dependency on nanowire diameter. TEM examination of the nanowire samples revealed that the density of stacking faults and thickness of ZB sections indeed varies between nanowires of different diameters but also varies substantially within individual nanowires. Nanowire bases exhibited higher densities of stacking faults and thicker ZB sections than nanowire tips. This large variability within individual nanowires precluded a complete quantitative analysis of how stacking fault density and ZB section thickness vary with nanowire diameter. Future contact-free measurements on InP nanowire samples (i) without planar crystallographic defects and (ii) with more well-defined defect densities should elucidate the dependence of mobility on stacking fault density and the thickness of ZB segments.

In this study, OPTP spectroscopy has revealed the effects of nanowire diameter, surfaces, and crystal structure on carrier dynamics in InP nanowires. Our measurements indicate that InP nanowire surfaces have only a weak influence on carrier lifetime, in marked contrast to GaAs nanowires. For InP nanowires the low surface recombination rate results in a long photoconductivity lifetime of over 1 ns, even without surface passivation. This long photoconductivity lifetime points to the immense technological potential of InP nanowires for future optoelectronic and photovoltaic devices. Furthermore, theoretical calculations and OPTP measurements demonstrated that InP nanowire surface roughness has a negligible effect on carrier mobility. The mobility is, however, significantly degraded by the presence of planar crystallographic defects. These defects are also responsible for the spatial separation of electrons and holes, which rapidly quenches nanowire PL. Future nanowire-based devices will therefore require very high crystal quality of constituent InP nanowires. This study shows the promise of even very narrow InP nanowires but emphasizes the importance of developing growth techniques to control InP nanowire crystal structure tightly and reproducibly.

■ ASSOCIATED CONTENT

Ⓢ Supporting Information

Description of experiments (nanowire growth, electron microscopy, terahertz time-domain spectroscopy, photoluminescence up-conversion spectroscopy), calculations for determining average nanowire diameter, calculations of nanowire surface area, calculations for determining surface recombination velocity, calculations for converting terahertz transmission data to photoconductivity, discussion of band bending at nanowire surfaces, discussion of ZB/WZ band offsets and thermal excitation, discussion of the fluence dependence of photoconductivity decay rates, calculation of theoretical carrier scattering rates, photoconductivity spectra at various times after photoexcitation, photoconductivity spectra for different nanowire diameters, and a summary of nanowire transport

E

dx.doi.org/10.1021/nl3026828 | Nano Lett. XXXX, XXX, XXX–XXX

parameters. This material is available free of charge via the Internet at http://pubs.acs.org.

■ AUTHOR INFORMATION

Corresponding Author
*E-mail: h.joyce1@physics.ox.ac.uk; m.johnston@physics.ox.ac.uk.

Notes
The authors declare no competing financial interest.

■ REFERENCES

(1) Wang, J. F.; Gudiksen, M. S.; Duan, X. F.; Cui, Y.; Lieber, C. M. *Science* **2001**, *293*, 1455−1457.

(2) Duan, X. F.; Huang, Y.; Cui, Y.; Wang, J. F.; Lieber, C. M. *Nature* **2001**, *409*, 66−69.

(3) Ding, Y.; Motohisa, J.; Hua, B.; Hara, S.; Fukui, T. *Nano Lett.* **2007**, *7*, 3598−3602.

(4) Goto, H.; Nosaki, K.; Tomioka, K.; Hara, S.; Hiruma, K.; Motohisa, J.; Fukui, T. *Appl. Phys. Express* **2009**, *2*, 035004.

(5) Novotny, C. J.; Yu, E. T.; Yu, P. K. L. *Nano Lett.* **2008**, *8*, 775−779.

(6) Franceschi, S. D.; van Dam, J. A.; Bakkers, E. P. A. M.; Feiner, L. F.; Gurevich, L.; Kouwenhoven, L. P. *Appl. Phys. Lett.* **2003**, *83*, 344−346.

(7) Joyce, H. J.; Gao, Q.; Tan, H. H.; Jagadish, C.; Kim, Y.; Zou, J.; Smith, L. M.; Jackson, H. E.; Yarrison-Rice, J. M.; Parkinson, P.; Johnston, M. B. *Prog. Quantum Electron.* **2011**, *35*, 23−75.

(8) Wallentin, J.; Ek, M.; Wallenberg, L. R.; Samuelson, L.; Borgström, M. T. *Nano Lett.* **2012**, *12*, 151−155.

(9) Maharjan, A.; Pemasiri, K.; Kumar, P.; Wade, A.; Smith, L. M.; Jackson, H. E.; Yarrison-Rice, J. M.; Kogan, A.; Paiman, S.; Gao, Q.; Tan, H. H.; Jagadish, C. *Appl. Phys. Lett.* **2009**, *94*, 193115.

(10) Parkinson, P.; Lloyd-Hughes, J.; Gao, Q.; Tan, H. H.; Jagadish, C.; Johnston, M. B.; Herz, L. M. *Nano Lett.* **2007**, *7*, 2162−2165.

(11) Casey, H. C.; Buehler, E. *Appl. Phys. Lett.* **1977**, *30*, 247−249.

(12) Nolte, D. D. *Solid-State Electron.* **1990**, *33*, 295−298.

(13) Léonard, F.; Talin, A. A.; Swartzentruber, B. S.; Picraux, S. T. *Phys. Rev. Lett.* **2009**, *102*, 106805.

(14) Dan, Y.; Seo, K.; Takei, K.; Meza, J. H.; Javey, A.; Crozier, K. B. *Nano Lett.* **2011**, *11*, 2527−2532.

(15) Diadiuk, V.; Groves, S. H.; Armiento, C. A.; Hurwitz, C. E. *Appl. Phys. Lett.* **1983**, *42*, 892−894.

(16) Rosenwaks, Y.; Shapira, Y.; Huppert, D. *Appl. Phys. Lett.* **1990**, *57*, 2552−2554.

(17) Parkinson, P.; Joyce, H. J.; Gao, Q.; Tan, H. H.; Zhang, X.; Zou, J.; Jagadish, C.; Herz, L. M.; Johnston, M. B. *Nano Lett.* **2009**, *9*, 3349−3353.

(18) Mattila, M.; Hakkarainen, T.; Lipsanen, H.; Jiang, H.; Kauppinen, E. I. *Appl. Phys. Lett.* **2007**, *90*, 033101.

(19) van Vugt; Veen, S. J.; Bakkers, E. P. A. M.; Roest, A. L.; Vanmaekelbergh, D. *J. Am. Chem. Soc.* **2005**, *127*, 12357−12362.

(20) Mattila, M.; Hakkarainen, T.; Mulot, M.; Lipsanen, H. *Nanotechnology* **2006**, *17*, 1580−1583.

(21) Mishra, A.; Titova, L. V.; Hoang, T. B.; Jackson, H. E.; Smith, L. M.; Yarrison-Rice, J. M.; Kim, Y.; Joyce, H. J.; Gao, Q.; Tan, H. H.; Jagadish, C. *Appl. Phys. Lett.* **2007**, *91*, 263104.

(22) Bao, J.; Bell, D. C.; Capasso, F.; Wagner, J. B.; Mårtensson, T.; Trägårdh, J.; Samuelson, L. *Nano Lett.* **2008**, *8*, 836−841.

(23) Murayama, M.; Nakayama, T. *Phys. Rev. B* **1994**, *49*, 4710−4724.

(24) De, S.; Coleman, J. N. *ACS Nano* **2010**, *4*, 2713−2720.

(25) Zhang, L.; Luo, J.; Zunger, A.; Akopian, N.; Zwiller, V.; Harmand, J. *Nano Lett.* **2010**, *10*, 4055−4060.

(26) van Weert, M. H. M.; Wunnicke, O.; Roest, A. L.; Eijkemans, T. J.; Silov, A. Y.; Haverkort, J. E. M.; 't Hooft, G. W.; Bakkers, E. P. A. M. *Appl. Phys. Lett.* **2006**, *88*, 043109.

(27) Pemasiri, K.; Montazeri, M.; Gass, R.; Smith, L. M.; Jackson, H. E.; Yarrison-Rice, J.; Paiman, S.; Gao, Q.; Tan, H. H.; Jagadish, C.; Zhang, X.; Zou, J. *Nano Lett.* **2009**, *9*, 648−654.

(28) Akopian, N.; Patriarche, G.; Liu, L.; Harmand, J. C.; Zwiller, V. *Nano Lett.* **2010**, *10*, 1198−1201.

(29) Nienhuys, H.-K.; Sundström, V. *Appl. Phys. Lett.* **2005**, *87*, 012101.

(30) Jancu, J. M.; Gauthron, K.; Largeau, L.; Patriarche, G.; Harmand, J. C.; Voisin, P. *Appl. Phys. Lett.* **2010**, *97*, 041910.

(31) Pitarke, J. M.; Silkin, V. M.; Chulkov, E. V.; Echenique, P. M. *Rep. Prog. Phys.* **2007**, *70*, 1−87.

(32) Seletskiy, D. V.; Hasselbeck, M. P.; Cederberg, J. G.; Katzenmeyer, A.; Toimil-Molares, M. E.; Léonard, F.; Talin, A. A.; Sheik-Bahae, M. *Phys. Rev. B* **2011**, *84*, 115421.

(33) Newman, N.; Spicer, W. E.; Kendelewicz, T.; Lindau, I. *J. Vac. Sci. Technol., B* **1986**, *4*, 931−938.

(34) Dreszer, P.; Chen, W. M.; Seendripu, K.; Wolk, J. A.; Walukiewicz, W.; Liang, B. W.; Tu, C. W.; Weber, E. R. *Phys. Rev. B* **1993**, *47*, 4111−4114.

(35) Razeghi, M.; Maurel, P.; Defour, M.; Omnes, F.; Neu, G.; Kozacki, A. *Appl. Phys. Lett.* **1988**, *52*, 117−119.

(36) Yu, P. Y.; Cardona, M. *Fundamentals of Semiconductors*, 3rd ed.; Springer: Berlin, 2005.

(37) Lloyd-Hughes, J. *Appl. Phys. Lett.* **2012**, *100*, 122103.

(38) Unuma, T.; Yoshita, M.; Noda, T.; Sakaki, H.; Akiyama, H. *J. Appl. Phys.* **2003**, *93*, 1586−1597.

(39) Storm, K.; Nylund, G.; Borgström, M.; Wallentin, J.; Fasth, C.; Thelander, C.; Samuelson, L. *Nano Lett.* **2011**, *11*, 1127−1130.

(40) Borgström, M. T.; Norberg, E.; Wickert, P.; Nilsson, H. A.; Trägårdh, J.; Dick, K. A.; Statkute, G.; Ramvall, P.; Deppert, K.; Samuelson, L. *Nanotechnology* **2008**, *19*, 445602.

(41) Paiman, S.; Gao, Q.; Tan, H. H.; Jagadish, C.; Pemasiri, K.; Montazeri, M.; Jackson, H. E.; Smith, L. M.; Yarrison-Rice, J. M.; Zhang, X.; Zou, J. *Nanotechnology* **2009**, *20*, 225606.

(42) Paiman, S.; Gao, Q.; Joyce, H. J.; Kim, Y.; Tan, H. H.; Jagadish, C.; Zhang, X.; Guo, Y.; Zou, J. *J. Phys. D-Appl. Phys.* **2010**, *43*, 445402.

Supporting Information for Ultra-low Surface Recombination Velocity in InP Nanowires Probed by Terahertz Spectroscopy

Hannah J. Joyce,[*,†] Jennifer Wong-Leung,[‡] Chaw-Keong Yong,[†] Callum J. Docherty,[†] Suriati Paiman,[‡,¶] Qiang Gao,[‡] H. Hoe Tan,[‡] Chennupati Jagadish,[‡] James Lloyd-Hughes,[†] Laura M. Herz,[†] and Michael B. Johnston[*,†]

Clarendon Laboratory, Department of Physics, University of Oxford, Oxford, OX1 3PU, UK, Department of Electronic Materials Engineering, Research School of Physics and Engineering, Australian National University, Canberra, ACT 0200, Australia, and Department of Physics, Faculty of Science, Universiti Putra Malaysia, 43400 Serdang, Selangor, Malaysia

E-mail: h.joyce1@physics.ox.ac.uk; m.johnston1@physics.ox.ac.uk

Experimental details

Growth

InP (111)B substrates were treated with poly-L-lysine. The substrate was cleaved into four portions and to each portion colloidal Au nanoparticles of a particular diameter (20, 30, 50 or 80 nm) were applied. Nanowires were grown at a pressure of 100 mbar and a total gas flow rate of 15 slm.

---

[*]To whom correspondence should be addressed
[†]Clarendon Laboratory, Department of Physics, University of Oxford, Oxford, OX1 3PU, UK
[‡]Department of Electronic Materials Engineering, Research School of Physics and Engineering, Australian National University, Canberra, ACT 0200, Australia
[¶]Department of Physics, Faculty of Science, Universiti Putra Malaysia, 43400 Serdang, Selangor, Malaysia

Growth was performed at 420°C for 20 minutes using trimethylindium and phosphine precursors with a V/III ratio of 700.

Electron microscopy and calculation of average nanowire diameters

Field emission scanning electron microscopy (FESEM) was carried out using a Hitachi S4300 FESEM at an accelerating voltage of 5 kV.

FESEM images of nanowires of quartz were used to quantify the nanowire diameter distributions of each of the four samples. For each sample, at least 50 individual nanowires were examined. For each individual nanowire, measurements of nanowire diameter were taken at approximately 250 nm intervals along the entire nanowire length. Using these data an average diameter was calculated for each nanowire. Each nanowire was binned according to its average diameter. The histograms were constructed by plotting the percentage of nanowires in each bin. The total nanowire length was also measured for each nanowire. The average diameter, $\bar{d}$, for each sample (namely 50 nm, 85 nm, 135 nm and 160 nm) was then calculated using the formula:

$$\bar{d} = \frac{\sum d_i l_i}{\sum l_i} \tag{S.1}$$

where d_i is the average diameter of nanowire i and l_i is its length.

For transmission electron microscopy (TEM) investigations, nanowires were first mechanically transferred to holey carbon grids. TEM was performed using a Phillips CM300 TEM operated at 300 kV. At least 5 nanowires were examined from each sample. Nanowires were examined for crystal structure and stacking faults over their entire length.

Terahertz time-domain spectroscopy

An amplified Ti:Sapphire laser with 4 W average power was used to generate 35 fs pulses centred at 800 nm at a 5 kHz repetition rate. Each pulse was split into three paths: approximately 590 μJ/pulse was used as the optical pump to photoexcite the sample, 200 μJ/pulse was used to generate the THz

probe pulse via optical rectification in a 2 mm GaP crystal, and 1.6 µJ/pulse was used as a gate for electro-optic detection of the transmitted THz pulse with a 200 µm GaP crystal. The optical pump beam was attenuated using neutral density filters to produce sample photoexcitation fluences between 1 and 160 µJ/cm^2. At the sample, the optical pump beamwidth had a full width at half maximum (FWHM) of 13 mm, whereas the THz probe FWHM was only 1.3 mm. Therefore the terahertz probe measured an area of approximately constant photoexcited carrier density. The THz electric field, E, was detected using a balanced photodiode circuit, and the signal was extracted using a lock-in amplifier referenced to a 2.5 kHz chopper in the THz generation beam. A second lock-in amplifier was used to detect the optical pump-induced change in terahertz electric field, ΔE, by referencing to a 125 Hz chopper in the optical pump beam. Varying the delay between the optical pump, terahertz probe and optical gate pulse produced a two-dimensional map of the THz spectral response of the material as a function of time after photoexcitation. The measurements were performed at room temperature with the entire terahertz beam path under vacuum, to avoid absorption of the terahertz radiation by atmospheric water vapour.

Photoluminescence up-conversion spectroscopy

The samples were excited at 736 nm using a mode-locked Ti:Sapphire laser oscillator supplying 100 fs pulses at a 82 MHz repetition rate. The spectral resolution of the time-resolved PL system at the selected detection wavelengths was 32 meV with a time-resolution of 200 fs. The PL was gated optically in a β-barium borate crystal using a fraction of the laser output that was subjected to an adjustable time delay with respect to the excitation pulse. Time-resolved PL measurements were recorded with a liquid-nitrogen cooled charge-coupled device (CCD) detector connected to a spectrometer.

Contribution of nanowire top and base to total surface area

We approximate the nanowire shape as a truncated cone with height, h, top diameter d_{top} and tapering angle, θ, as illustrated in Figure S.1a. The top surface area is given by

$$\pi r_{\text{top}}^2, \tag{S.2}$$

where $r_{\text{top}} = \frac{1}{2} d_{\text{top}}$. The bottom surface area is given by

$$\pi \left(r_{\text{top}} + h \tan \theta \right)^2. \tag{S.3}$$

The surface area made up by the lateral side surfaces is given by

$$\frac{\pi h}{\cos \theta} \left(2 r_{\text{top}} + h \tan \theta \right). \tag{S.4}$$

The summation of these three terms, S.2 to S.4, gives the total surface area. The sum of terms S.2 and S.3 gives the contribution of the top and bottom faces to the total surface area. Figure S.1b plots the proportion of the total surface area due to the sum of the top and bottom surfaces, as a function of nanowire aspect ratio, h/d_{top}. The data for four different tapering angles, θ, were plotted. The tapering angle $\theta = 0$ corresponds to an untapered cylinder. The remaining three tapering angles are typical of the nanowires of our study. The range of aspect ratios plotted is also typical of the nanowires of our study. It is clear from Figure S.1b that the top and bottom surfaces make only a small contribution to the total surface area, whereas the lateral side surfaces make the dominant contribution to total nanowire surface area. We therefore we may neglect the top and bottom surfaces in our analysis, and focus on the dependence of carrier lifetime as a function of nanowire diameter.
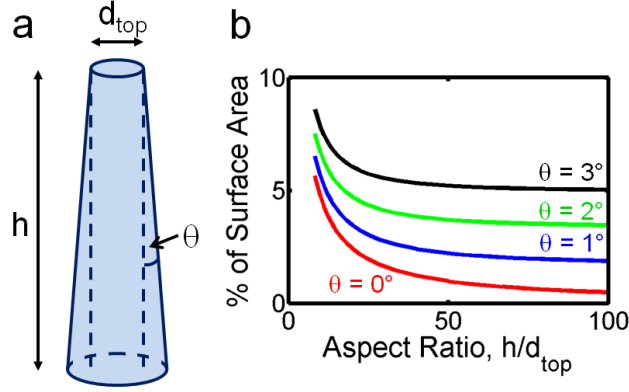
Figure S.1: (a) Schematic of a truncated cone, illustrating the parameters defining the nanowire shape: height, h, top diameter, d_{top}, and tapering angle, θ. (b) Plot of the contribution made by the sum of nanowire top surface and base surface to the total surface area.

Calculation of surface recombination velocity

To calculate the surface recombination velocity, we have followed the methods derived by Léonard *et al.* and Dan *et al.*[1,2] The nanowire geometry is approximated as a cylinder of infinite length, for which the continuity equation describing the carrier concentration profile is given by

$$\frac{\partial (\Delta n)}{\partial t} = D \frac{\partial^2 (\Delta n)}{\partial r^2} - \frac{\Delta n}{\tau_{volume}}, \tag{S.5}$$

where Δn is the photoexcited electron density, D is the diffusion constant, r is the radial coordinate and τ_{volume} is the electron lifetime in bulk InP. This continuity equation is subject to the boundary conditions:

$$D \frac{\partial (\Delta n)}{\partial r}\Big|_{r=\frac{d}{2}} = -S\Delta n, \tag{S.6}$$

where d is the nanowire diameter and S is the surface recombination velocity. Solution of the continuity equation gives an exponential time decay of the carrier density with the following expression for carrier lifetime:

$$\frac{1}{\tau} = \frac{1}{\tau_{volume}} + \frac{4\beta^2 D}{d^2}, \tag{S.7}$$

5

In the above equation, β is given by

$$\beta J_1(\beta) - L J_0(\beta) = 0, \tag{S.8}$$

where J_0 and J_1 are 0th and 1st order Bessel functions of the first kind and

$$L = \frac{dS}{2D}. \tag{S.9}$$

For small β we can use the small argument behaviour of Bessel functions:

$$J_n(\beta) \approx \frac{1}{2^n n!} \beta^n, \tag{S.10}$$

so that $J_0(\beta) = 1$ and $J_1(\beta) = \frac{1}{2}\beta$. Substituting these values into Equation (S.8) gives $\beta = \sqrt{2L}$. Using this approximation, Equation (S.7) simplifies to

$$\frac{1}{\tau} = \frac{1}{\tau_{\text{volume}}} + \frac{4S}{d}. \tag{S.11}$$

Equation (S.11) was then fitted to the monoexponential decay lifetimes ($\tau = 1.18\,\text{ns}$, $1.27\,\text{ns}$, $1.30\,\text{ns}$ and $1.34\,\text{ns}$) of the four samples ($d = 50$, 85, 135 and 160 nm, respectively), as plotted in Figure S.2. This yielded τ_{volume} of $1.4\,\text{ns}$ and a surface recombination velocity of $170\,\text{cm/s}$.
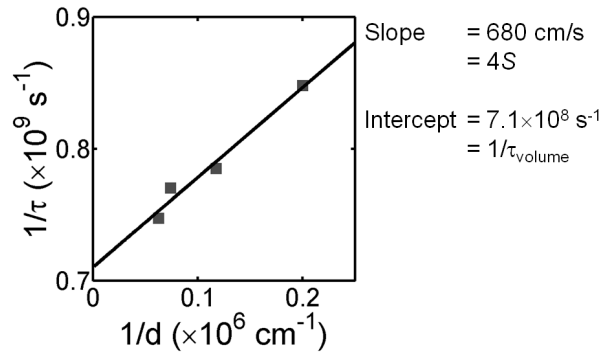

Figure S.2: Plot of decay rate, $\frac{1}{\tau}$, against inverse nanowire diameter, $\frac{1}{d}$. This plot was used to extract the surface recombination velocity, S, and bulk recombination lifetime, τ_{volume}. Square symbols represent the monoexponential decay lifetimes for the four samples of different diameter. The black line is the line of best fit to Equation (S.11).

6

To confirm that the initial approximation of small β is valid, we verify that $L = \frac{dS}{2D} \ll 1$, as follows. The minimum diffusion constant is calculated using the Einstein relation and inserting the lowest measured mobility of $120\,\mathrm{cm^2 V^{-1} s^{-1}}$:

$$D = \frac{\mu k_B T}{e} = 3.1\,\mathrm{cm^2 s^{-1}}. \tag{S.12}$$

The maximum nanowire diameter is $160\,\mathrm{nm}$ and $S = 170\,\mathrm{cm/s}$. Therefore $L = \frac{dS}{2D} < 4.4 \times 10^{-4}$, so $L \ll 1$ and Equation (S.11) is valid.

Conversion of terahertz transmission data to photoconductivity

This section outlines how photoconductivity $\Delta\sigma$ is extracted from our OPTP measurement of $\frac{\Delta E}{E}$.

Using SEM images of nanowires on quartz, we calculated the effective areal fill factor of nanowires, f_w, for each sample. We consider the nanowires to be embedded within the surrounding vacuum, within a layer of thickness δ. The transmitted terahertz electric fields with and without the optical pump are defined as

$$
\begin{aligned}
E_{\mathrm{on}} &= f_w E_{w^*} + (1 - f_w) E_v \tag{S.13} \\
E_{\mathrm{off}} &= f_w E_w + (1 - f_w) E_v, \tag{S.14}
\end{aligned}
$$

where E_w and E_v are the terahertz transmission through the nanowires and the surrounding vacuum, respectively, and * indicates a photoexcited state. Note that the pump beam does not change the complex refractive index of the vacuum. The electric fields E_v, E_w and E_{w^*} may then be written as

$$
\begin{aligned}
E_v &= e^{in_v \omega \delta / c} E_i \tag{S.15} \\
E_w &= t_{vw} t_{wv} e^{in_w \omega \delta / c} \mathrm{FP}_{vwv} E_i \tag{S.16} \\
E_{w^*} &= t_{vw^*} t_{w^* v} e^{in_{w^*} \omega \delta / c} \mathrm{FP}_{vw^* v} E_i, \tag{S.17}
\end{aligned}
$$

7

where FP_{ijk} are the Fabry-Pérot terms, t_{ij} are the Fresnel transmission coefficients, c is the speed of light in vacuum, and n_{w^*} and n_{w} are the refractive indices of nanowires with and without photoexcitation, respectively.

Combining Equations (S.13) and (S.14) gives

$$\frac{E_{\mathrm{w}^*}}{E_{\mathrm{w}}} = \frac{\Delta E}{E}\left[1 + \left(\frac{1}{f_{\mathrm{w}}} - 1\right)\frac{E_{\mathrm{v}}}{E_{\mathrm{w}}}\right] + 1, \tag{S.18}$$

where $\Delta E = E_{\mathrm{on}} - E_{\mathrm{off}}$. Note that the OPTP system gives direct experimental measurement of $\frac{\Delta E}{E}$ where ΔE is the photoinduced change in terahertz probe transmission and $E = E_{\mathrm{off}}$ is the terahertz probe transmission in the absence of photoexcitation.

At terahertz frequencies the thin film limit is valid because $\frac{n\omega\delta}{c} \ll 1$. In the thin film limit we can make the approximation $\frac{E_{\mathrm{v}}}{E_{\mathrm{w}}} = 1$. Using this approximation and rearranging Equation (S.18), we define parameter A as

$$A = \frac{E_{\mathrm{w}}}{E_{\mathrm{w}^*}} = \frac{1}{\frac{1}{f_{\mathrm{w}}}\frac{\Delta E}{E} + 1}. \tag{S.19}$$

Substituting the appropriate forms of FP_{ijk} and t_{ij} into Equations (S.15) to (S.17) and applying the thin film limit $e^{in\omega\delta/c} = 1 + in\omega\delta/c$ gives

$$\frac{E_{\mathrm{w}^*}}{E_{\mathrm{w}}} = \frac{2 - \frac{i\omega\delta}{c}(1 + n_{\mathrm{w}}^2)}{2 - \frac{i\omega\delta}{c}(1 + n_{\mathrm{w}^*}^2)}, \tag{S.20}$$

The following general relations can then be substituted into Equation (S.20)

$$n_{\mathrm{w}}^2 = \varepsilon_{\mathrm{w}} \tag{S.21}$$

$$n_{\mathrm{w}^*}^2 = \varepsilon_{\mathrm{w}^*} \tag{S.22}$$

to give

$$\varepsilon_{w*} = \left[-\frac{E_w}{E_{w*}} \left(2\frac{c}{i\omega\delta} - (1+\varepsilon_w) \right) + 2\frac{c}{i\omega\delta} - 1 \right], \tag{S.23}$$

where ε_{w*} and ε_w are the dielectric constants of the nanowires with and without photoexcitation, respectively. The photoinduced conductivity, $\Delta\sigma$, is given by

$$\varepsilon_{w*} = \varepsilon_w + \frac{i\Delta\sigma}{\omega\varepsilon_0}, \tag{S.24}$$

where ε_0 is the permittivity of free space. Substituting Equation (S.23) into Equation (S.24) gives the following expression for $\Delta\sigma$ in terms of the measured signal $\frac{\Delta E}{E}$:

$$\Delta\sigma = \varepsilon_0 (A-1) \left[\frac{2c}{\delta} - i\omega (1+\varepsilon_w) \right], \tag{S.25}$$

where A is defined in Equation (S.19). Thus, using Equations (S.25) and (S.19), the measured signal can be converted to $\Delta\sigma$ using $\varepsilon_w = 12.5$ as for bulk InP and values of f_w and δ as measured from SEM images.

Spatial separation due to band-bending at nanowire surfaces

An alternative mechanism for spatial separation of electrons and holes concerns band bending at the nanowire surface. Band bending effects have been observed in semiconductor structures with high surface area-to-volume ratios such as p-type InP nanowires,[3] Ge nanowires[4] and porous InP.[5] In InP, surface states tend to pin the Fermi level within 0 to 0.34 eV of the conduction band edge, depending on the crystallographic orientation of the surface.[6,7] It is reasonable to assume that the nanowire side facets, which are predominantly $\{1\bar{1}00\}$ oriented, will experience surface Fermi level pinning near the conduction band edge. Assuming the InP is doped at 5.5×10^{16} cm^{-3} (as justified in the main manuscript), the Fermi level pinning creates band bending such that the electrons become confined to the surface and the holes to the centre of the nanowire. At early times after photoexcitation the carrier density would screen this surface field, reducing band bending and

increasing the likelihood of electron–hole recombination. Consequently, PL would be observed at early times. At later times, however, when the carrier density is lower, the surface field would result in spatial separation of electrons and holes, which would suppress radiative recombination and would account for the rapid quenching of PL at 1.43 eV.

A study by van Weert *et al.*, however, demonstrated that band-bending effects are only pronounced in p-InP nanowires.[3] The nanowires of our study are thought to be n-type, and exhibited a very low surface recombination velocity, indicating that band-bending effects are negligible. Therefore presence of stacking faults and ZB/WZ polytypism is more likely to account for our observations of a short PL lifetime coupled with a long photoconductivity lifetime.

Spatial separation due to ZB/WZ band offsets

In WZ InP, the conduction band is approximately 129 meV higher in energy, and the valence band is approximately 45 meV higher in energy, than in ZB InP. ZB sections within a nanowire are therefore potential wells for electrons, whereas WZ sections are potential wells for holes. Due to quantum confinement, electrons and holes occupy discrete energy levels within these wells, with the energy level depending on the thickness of the well. We calculated the eigenstates of finite square wells to determine these energy levels as a function of well thickness. As the WZ sections in these nanowires are typically thick, the hole states will lie at, or near the WZ valence band edge, 45 meV above the ZB valence band edge. This is significantly higher than the thermal energy at room temperature, $k_B T = 26$ meV, so there should be little thermal excitation of holes out of the WZ potential wells. The ZB sections occur at higher densities at the nanowire bases, where they are typically 1 nm to 3 nm in width. For ZB wells 2 nm in width, the lowest lying energy state is 29 meV below the WZ conduction band edge. This is above the thermal energy at room temperature, $k_B T = 26$ meV. Therefore, for ZB potential wells greater than 2 nm in thickness, there should be little thermal excitation of electrons at room temperature. For ZB sections less than 2 nm in thickness, however, the electrons are only weakly localized.

Photoexcited carrier density

The photoexcited carrier density, N_p, within a sample of thickness d is given by

$$N_p = \frac{I}{Ed}\left(1 - e^{-d/\alpha}\right),$$

(S.26)

where I is the photoexcitation fluence, α is the absorption depth and E is the photon energy. At our photoexcitation wavelength of $\lambda = 800\,\mathrm{nm}$, $\alpha = 400\,\mathrm{nm}$ for InP. This α is significantly larger than all the nanowire diameters we studied, which places the nanowires in the thin film limit. This means that for a given photoexcitation intensity, the photoexcited carrier density is approximately constant regardless of nanowire diameter.

Fluence dependence of photoconductivity decay rate

Figure S.3 shows the decays of $\Delta E / E$ with time after photoexcitation for two different InP nanowire samples: 50 nm diameter and 135 nm diameter. From Figure S.3 it is evident that the decay lifetime is approximately constant at all photoexcitation fluences. Similarly, the other two samples, of 85 nm and 160 nm diameter, showed constant decay lifetimes regardless of photoexcitation fluence. This indicates that the carrier lifetime is minimally affected by the carrier density.
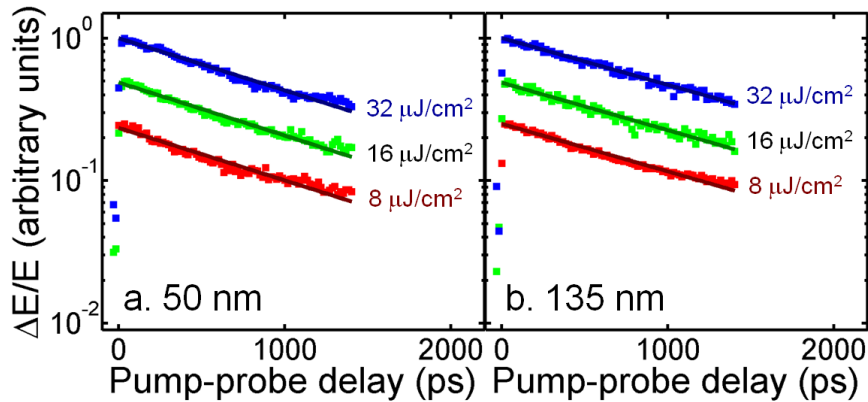

Figure S.3: Pump-induced change in terahertz electric field ($\Delta E / E$) at different pump–probe delays, for (a) 50 nm and (b) 135 nm diameter InP nanowires. Results for three different photoexcitation fluences are plotted: 8, 16 and 32 μJ/cm^2.

11

Calculation of theoretical scattering rates in bulk InP

Theoretical scattering rates for bulk InP are plotted in the dotted curve of Figure 4g. These scattering rates were calculated assuming parameters for bulk ZB InP, such as phonon frequency and $m_e^* = 0.08 m_e$. Electron–phonon, electron–electron, electron–hole and electron–plasmon mechanisms were included in the rates. The calculation follows published models.[8,9] Carrier distributions were assumed to be thermalised and at room temperature. An ionised donor density of $5.5 \times 10^{16}\,\mathrm{cm}^{-3}$ was assumed for calculation of electron–impurity scattering. Electron–phonon scattering dominates the calculated scattering rates at low carrier density and is roughly independent of carrier density. The rates for electron–electron, electron–hole and electron–plasmon scattering increase with carrier density.

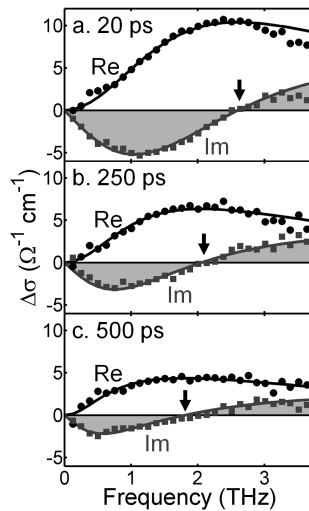# Photoconductivity spectral evolution

Figure S.4: Time-resolved conductivity of photoexcited carriers in 50 nm InP nanowires at times (a) 20 ps, (b) 250 ps and (c) 500 ps after the pump excitation pulse. The symbols are the measured data and the lines are the fitted plasmon responses. The real (circles and lines) and imaginary (squares and lines) components of the conductivity are plotted. The incident pump pulse fluence was $10\,\mu\mathrm{J/cm}^2$. The arrow indicates the resonant surface plasmon frequency ω_0.

Figure S.4 shows photoconductivity spectra of 50 nm nanowires taken various times after pho-

toexcitation. The surface plasmon resonance shifts to lower frequencies with time, reflecting the decay in carrier density with time.

Photoconductivity spectra of nanowires of different diameter
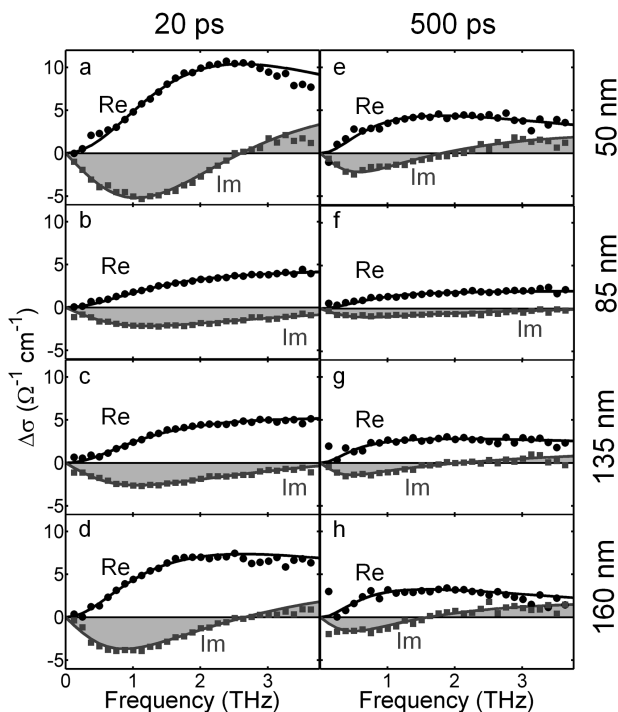

Figure S.5: Conductivity of photoexcited carriers in (a, e) 50, (b, f) 85, (c, g) 135 and (d, h) 160 nm diameter InP nanowires at (a-d) 20 ps after photoexcitation and (e-h) 500 ps after photoexcitation with a pump pulse of fluence $10 \, \mu J/cm^2$. The symbols are the measured data and the lines are the fitted plasmon responses. The real (circles and lines) and imaginary (squares and lines) components of the conductivity are plotted.

Figure S.5 shows photoconductivity spectra taken for the four different nanowire samples of 50, 85, 135 and 160 nm diameter. These spectra were measured at 20 ps and 500 ps after photoexcitation with a pump fluence of $10 \, \mu J/cm^2$. The extracted scattering rates and mobilities are summarized in Table S.1. After photoexcitation, the photoexcited carrier density decays. As the photoexcited carrier density decays, the scattering rate exhibits a small decrease, because carrier–carrier scattering decreases.

At 20 ps after photoexcitation, the extracted scattering rates were $3.3 \times 10^{13} \, s^{-1}$, $18 \times 10^{13} \, s^{-1}$,

$10 \times 10^{13} \, \text{s}^{-1}$ and $4.5 \times 10^{13} \, \text{s}^{-1}$ respectively for the 50, 85, 135 and 160 nm diameter nanowires. These scattering rates correspond to mobilities of 660, 120, 220 and $480 \, \text{cm}^2 \text{V}^{-1} \text{s}^{-1}$. In the data of Table S.1, we observe only a weak dependence of mobility on time after photoexcitation. Therefore these mobility values are valid for a wide range of carrier densities.

Table S.1: Electron scattering rates (γ) and mobilities (μ) extracted from the spectra of Figure S.5 for the four nanowire samples of different diameter (d).

Diameter, d (nm)	Pump–probe delay (ps)	γ (s^{-1})	μ $(\text{cm}^2\text{V}^{-1}\text{s}^{-1})$
50 nm	20 ps	3.3×10^{13}	660
	500 ps	3.1×10^{13}	700
85 nm	20 ps	18×10^{13}	120
	500 ps	17×10^{13}	130
135 nm	20 ps	10×10^{13}	220
	500 ps	9.0×10^{13}	260
160 nm	20 ps	4.5×10^{13}	480
	500 ps	4.2×10^{13}	530

Transport parameters for InP nanowires

Table S.2 summarises the transport parameters extracted from the OPTP measurements on the four samples of 50, 85, 135 and 160 nm diameter. The photoexcited carrier lifetime, τ, was inferred from the photoconductivity decays of Figure 2a. The electron scattering rate, γ, was extracted from the spectra of Figure S.5. Using τ and γ, quantities for the electron mobility (μ), mean free path (λ), diffusion constant (D) and diffusion length (L) were calculated using

$$\mu = \frac{e}{m_{\text{e}}^* \gamma} \tag{S.27}$$

$$\lambda = v\tau \tag{S.28}$$

$$D = \frac{\mu k_{\text{B}} T}{e} \tag{S.29}$$

$$L = \sqrt{D\tau} \tag{S.30}$$

14

where e is the electronic charge, m_{e}^{*} is the electron effective mass, v is the electron thermal velocity at room temperature and k_{B} is the Boltzmann constant. We deduce v by solving the equation

$$E = \frac{1}{2}m_{\mathrm{e}}^{*}v^2 = \frac{3}{2}k_{\mathrm{B}}T \tag{S.31}$$

to give $v = 4.1 \times 10^5 \, \mathrm{ms}^{-1}$.

Table S.2: Parameters extracted for the four nanowire samples of different diameter (d), including photoexcited carrier lifetime (τ), electron scattering rate (γ), electron mobility (μ), mean free path (λ), diffusion constant (D) and diffusion length (L).

d (nm)	τ (ns)	γ (s^{-1})	μ ($\mathrm{cm}^2\mathrm{V}^{-1}\mathrm{s}^{-1}$)	λ (nm)	D ($\mathrm{cm}^2\mathrm{s}^{-1}$)	L (nm)
50	1.18	3.3×10^{13}	660	12	17	1400
85	1.27	18×10^{13}	120	2.3	3.1	630
135	1.30	10×10^{13}	220	4.1	5.7	860
160	1.34	4.5×10^{13}	480	9.1	13	1300

References

(1) Léonard, F.; Talin, A. A.; Swartzentruber, B. S.; Picraux, S. T. *Phys. Rev. Lett.* **2009**, *102*, 106805.

(2) Dan, Y.; Seo, K.; Takei, K.; Meza, J. H.; Javey, A.; Crozier, K. B. *Nano Lett.* **2011**, *11*, 2527–2532.

(3) van Weert, M. H. M.; Wunnicke, O.; Roest, A. L.; Eijkemans, T. J.; Silov, A. Y.; Haverkort, J. E. M.; 't Hooft, G. W.; Bakkers, E. P. A. M. *Appl. Phys. Lett.* **2006**, *88*, 043109.

(4) Prasankumar, R. P.; Choi, S.; Trugman, S. A.; Picraux, S. T.; Taylor, A. J. *Nano Lett.* **2008**, *8*, 1619–1624.

(5) Lloyd-Hughes, J.; Mueller, S.; Scalari, G.; Bishop, H.; Crossley, A.; Enachi, M.; Sirbu, L.; Tiginyanu, I. M. *Appl. Phys. Lett.* **2012**, *100*, 132106.

(6) Koenders, L.; Bartels, F.; Ullrich, H.; Monch, W. *J. Vac. Sci. Technol. B* **1985**, *3*, 1107–1115.

(7) Moison, J. M.; Bensoussan, M. *Surf. Sci.* **1986**, *168*, 68–73.

(8) Yu, P. Y.; Cardona, M. *Fundamentals of Semiconductors*, 3rd ed.; Springer, Berlin, 2005.

(9) Lloyd-Hughes, J. *Appl. Phys. Lett.* **2012**, *100*, 122103.